Using Acoustic Travel Time to Monitor the Heat Variability of Glacial Fjords

ROBERT SANCHEZ,[a] FIAMMA STRANEO,[a] AND MAGDALENA ANDRES[b]

[a] *Scripps Institution of Oceanography, University of California, San Diego, San Diego, California*
[b] *Woods Hole Oceanographic Institution, Woods Hole, Massachusetts*

(Manuscript received 29 October 2020, in final form 9 June 2021)

ABSTRACT: Monitoring the heat content variability of glacial fjords is crucial to understanding the effects of oceanic forcing on marine-terminating glaciers. A pressure-sensor-equipped inverted echo sounder (PIES) was deployed midfjord in Sermilik Fjord in southeast Greenland from August 2011 to September 2012 alongside a moored array of instruments recording temperature, conductivity, and velocity. Historical hydrography is used to quantify the relationship between acoustic travel time and the vertically averaged heat content, and a new method is developed for filtering acoustic return echoes in an ice-influenced environment. We show that PIES measurements, combined with a knowledge of the fjord's two-layer density structure, can be used to reconstruct the thickness and temperature of the inflowing water. Additionally, we find that fjord–shelf exchange events are identifiable in the travel time record implying the PIES can be used to monitor fjord circulation. Finally, we show that PIES data can be combined with moored temperature records to derive the heat content of the upper layer of the fjord where moored instruments are at great risk of being damaged by transiting icebergs.

KEYWORDS: Glaciers; Ice sheets; Acoustic measurements/effects; In situ oceanic observations

1. Introduction

Under sustained global warming the Greenland Ice Sheet is predicted to continue losing mass during the twenty-first century with consequences for sea level rise (Bamber et al. 2019; Goelzer et al. 2020). Changes in the oceanic heat available for melting are thought to be one of the main drivers of glacial retreat (Holland et al. 2008; Motyka et al. 2011; Straneo and Heimbach 2013; Khazendar et al. 2019). The amount of heat available for melting, in turn, depends on the hydrographic properties of fjords, which connect marine-terminating glaciers with the continental shelf (Straneo et al. 2012). However, our knowledge of the variability of ocean properties in glacial fjords is limited by the challenges of maintaining consistent, multiyear observations (Straneo et al. 2016, 2019). Since ocean circulation models presently cannot resolve fjords, long-term measurements are key to mapping and building an understanding of the physical mechanisms controlling fjord variability.

The melt rate of a glacier is set by heat fluxes across the ice–ocean boundary layer. These heat fluxes are a function of ocean temperatures and velocities near the glacier, and are influenced by both the local release of subglacial discharge and the large-scale fjord circulation (Jenkins 2011; Slater et al. 2018; Sutherland et al. 2019; Jackson et al. 2020). Thus, to diagnose heat content variability and infer melt-rate variability, observations are needed of both fjord water-mass properties and fjord circulation (Straneo et al. 2019). Of primary interest is knowing the heat content of the inflowing water at roughly the grounding line depth of the glacier, which induces submarine melting and has been correlated to changes in ice discharge (Holland et al. 2008; Motyka et al. 2011; Luckman et al. 2015; Khazendar et al. 2019). Additionally, measurements are needed of near-ice velocities, which ultimately transfer heat across the ice–ocean boundary layer and have recently been shown to significantly affect glacial melt rates (Slater et al. 2019; Sutherland et al. 2019; Jackson et al. 2020). Last, far-field monitoring of the large-scale fjord circulation is needed to quantify the variability of the heat transport toward the glacier and renewal within the fjord (Straneo et al. 2011; Jackson et al. 2020). Measurements of these desired variables are presently limited due to the extreme challenges of working in glacial fjords.

Monitoring Greenland's glacial fjords is difficult because of the high costs of operating in such remote and hazardous environments (Straneo et al. 2019). Ocean measurements have been primarily limited to the summer when weather conditions are less harsh and the fjords more navigable. While moorings have had some success in capturing the temporal variability of fjords (Mortensen et al. 2014; Jackson and Straneo 2016; Carroll et al. 2018; Boone et al. 2018), their effectiveness is often limited because of icebergs that have deep keels, which can extend down hundreds of meters (Straneo et al. 2016). To avoid destruction, the topmost flotation and instruments on a mooring are typically far below the surface or confined to a shallow embayment. Because of the challenges of observing glacial fjords, a diverse set of instruments and measuring techniques are required.

One potential approach for measuring the heat content variability of glacial fjords without succumbing to damage from icebergs is to use bottom-mounted acoustic devices. Bottom-to-surface round-trip acoustic travel time is an integrated measurement that depends on the depth and sound speed properties of the water column (Del Grosso 1974). Since the speed of sound in seawater is primarily a function of

Supplemental information related to this paper is available at the Journals Online website: https://doi.org/10.1175/JTECH-D-20-0176.s1.

Corresponding author: Robert Sanchez, rmsanche@ucsd.edu

DOI: 10.1175/JTECH-D-20-0176.1

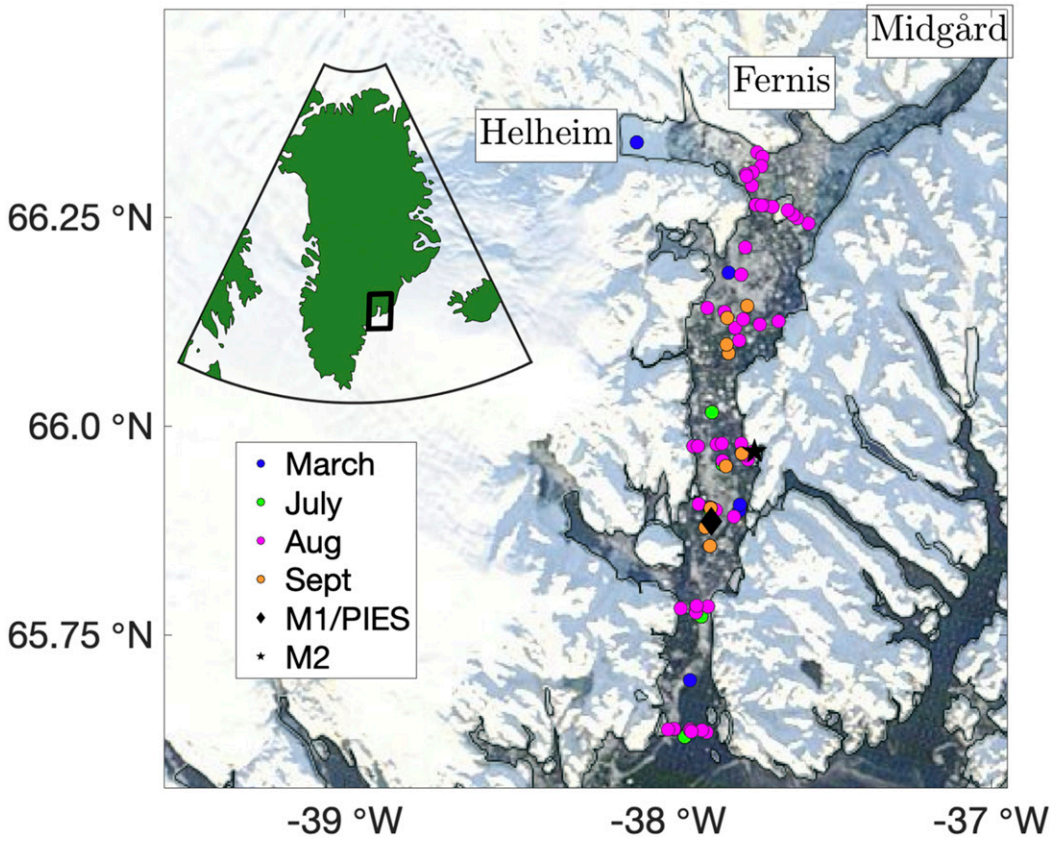

FIG. 1. A map of Sermilik Fjord, which shows the locations of all the CTD profiles collected as well as the locations of the moorings and PIES. The inset shows the fjord's location with respect to the Greenland continent. The glacier locations of Helheim, Fernis, and Midgård are also labeled.

temperature, acoustic travel time over a fixed depth is proportional to the integrated heat content of the overlying water (Watts and Rossby 1977).

In this study, we investigate the potential use of acoustic travel time to monitor fjord properties relating to glacial melt variability, such as heat content, through observations collected in Sermilik Fjord (SF) in southeast Greenland. Using hydrographic data, we show that seasonal and interannual changes in integrated heat content are associated with a measurable signal in acoustic travel time (section 2). We provide a description of how to process acoustic travel time data in an ice-influenced environment (section 3). Next, acoustic travel time data collected in SF with a pressure-sensor-equipped inverted echo sounder (PIES) deployed on the seabed alongside a traditional oceanographic mooring are used to investigate the extent to which PIES measurements can diagnose quantities that are relevant to studies of fjord circulation and fjord variability (section 4). We show that acoustic travel time can be used to infer the thickness and temperature of the deep, warm inflowing water in the winter (section 4a), track fjord circulations that are associated with shifts in the pycnocline (section 4b), and remotely measure the heat content of the top layer of the fjord (section 4c). We finish with a discussion of potential challenges and benefits of using PIES to monitor glacial fjords (section 5).

2. Regional setting and theory

a. *Hydrographic properties of Sermilik Fjord*

We first investigate acoustic travel time using hydrographic data collected in SF in southeast Greenland. The fjord connects Helheim Glacier, the fifth largest outlet glacier of the Greenland Ice Sheet and two smaller glaciers, Midgård and Fernis, to the continental shelf (Fig. 1). The Helheim–Sermilik system is one of the most well-studied glacial fjord environments in Greenland with continuous measurements since 2008 (Straneo et al. 2016). The fjord is 550–900 m deep and about 75–100 km long and varies in width from 5 to 10 km. The fjord, like the adjacent continental shelf, is composed of cold and fresh polar water (PW) from the Arctic over relatively warm and salty Atlantic Water (AW) from the Irminger Sea.

Conductivity–temperature–depth (CTD) profiles were collected throughout SF in the summers of 2011–17, and expendable CTDs (XCTD) were deployed by helicopter in the winter of March 2010 (Table 1). In the winter, the fjord's density structure resembles two layers with cold and fresh PW [Conservative Temperature (Θ) $<$ 0°C, Absolute Salinity

TABLE 1. Details of XCTD and CTD collection dates and previously published data.

Instrument	Data collection time	Previously published
XCTD	March 2010	Straneo et al. (2011)
CTD	August 2011, September 2012, August 2013	Jackson and Straneo (2016)
CTD	August 2015	Beaird et al. (2018), Cape et al. (2019)
CTD	July 2017	Unpublished

(S_A) < 33.3 g kg^{-1}] above relatively warm and salty AW (Θ > 3°C, S_A > 34.7g kg^{-1}) (Figs. 2a,b) (Straneo et al. 2010). The two water masses can be characterized as weakly stratified "layers" separated by a sharp pycnocline centered around 200 m depth. In the summer, the fjord stratification and temperature structure is more complex due to the presence of a third water mass, a mixture of meltwater and ocean water called glacially modified water (GMW; Figs. 2a,b) (Beaird et al. 2018). In SF, GMW appears as a relatively warm and salty intrusion in the upper 250 m due to the entrainment and upwelling of deep AW by buoyant freshwater released at depth (Straneo et al. 2010, 2011). However, above 50 m, GMW appears as a relatively fresh anomaly due to the increased concentration of freshwater toward the surface (Straneo et al. 2011; Beaird et al. 2018). The casts taken during the summers show that both inflowing AW and exported GMW temperatures can vary by over 1°C interannually. The sound speed derived from the mean hydrographic profiles generally increases with depth and resembles the temperature profiles (Fig. 2c).

b. Relationship between travel time and heat content

Travel time (τ) is expressed by

$$\tau = 2\int_{-H}^{\eta_s} \frac{1}{c(z)}\,dz, \tag{1}$$

where H is the seafloor depth (m), η_s is the sea surface height (m), $c(z)$ is the speed of sound (m s^{-1}), and the 2 arises because τ is a round-trip travel time. Since sound speed is approximately proportional to temperature, from (1) we expect acoustic travel time to be approximately proportional to integrated heat content (Watts and Rossby 1977). However, glacial fjords have large vertical and horizontal density gradients due to significant freshwater input that can potentially affect c and therefore τ. Thus, we first test our hypothesis that τ is proportional to integrated heat content in glacial fjords by using the hydrographic profiles (Table 1).

The CTD casts were primarily taken during the summer months (July–September), and XCTD casts were collected during a rare winter survey (March 2010). The temporal coverage, in addition to the spatial variability within the fjord

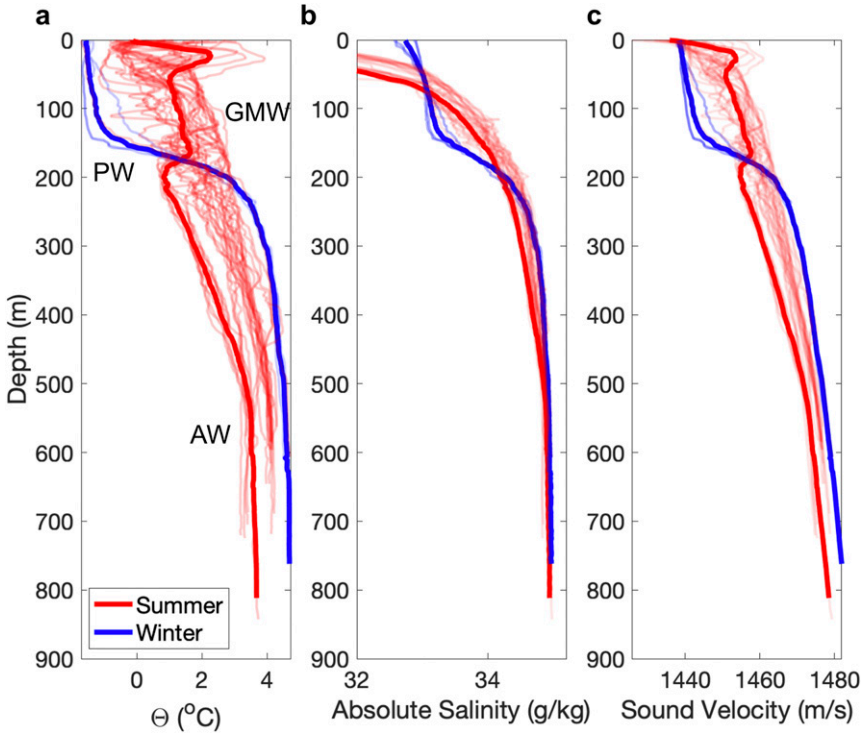

FIG. 2. CTD profiles collected in Sermilik Fjord from 2010 to 2017. In red (blue) are those profiles collected in summer (winter). The bold blue is from March 2010 and the bold red is September 2012 (when the PIES was recovered). (a) Conservative Temperature, (b) Absolute Salinity, and (c) sound velocity.

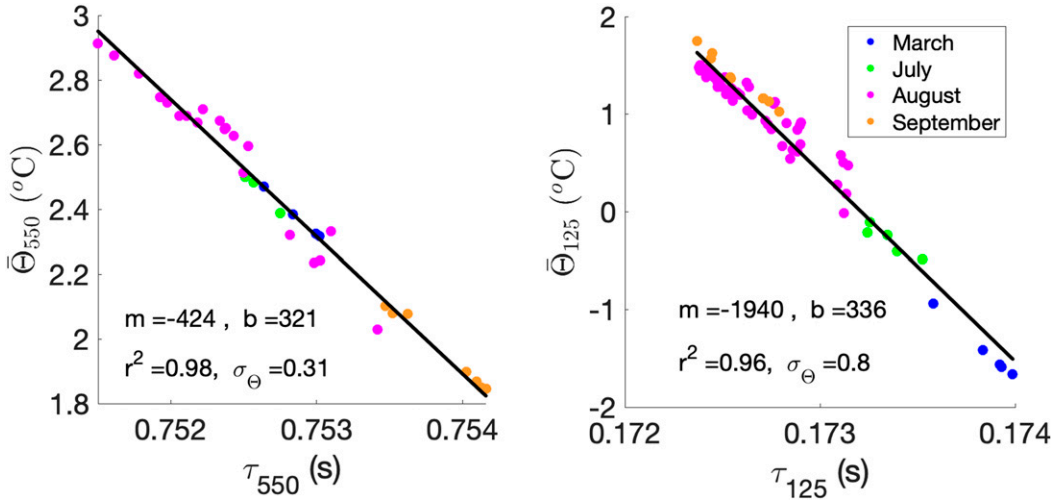

FIG. 3. (a) Travel time calculated from the surface down to 550 m against the average Conservative Temperature over the same depth range. Colors indicate month. (b) As in (a), but down to 125 m.

(Fig. 1), provides a useful range of property distribution that allows us to test the relationship between travel time and water column temperature. From each CTD/XCTD profile, we derive the sound speed profile (Roquet et al. 2015) and subsequently integrate it to produce τ according to (1). Variations in the calculated travel time are then compared to the integrated heat content, here estimated by the vertically averaged Conservative Temperature ($\overline{\Theta}$) for each cast (Figs. 3a,b). We find that there exists a strong linear relationship between τ and $\overline{\Theta}$ over both 125 m ($r^2 = 0.96$) and 550 m ($r^2 = 0.98$).

Since SF, like most glacial fjords, experiences significant salinity gradients both spatially and temporally, we examine the impact of salinity on our interpretation of travel time by estimating how $\overline{\Theta}$—predicted from τ—would differ if a mean salinity profile was used in place of the observed salinity. We find that τ has an average error of 0.14 ms if calculated using a mean salinity profile from all CTD casts (hereafter denoted with a subscript μ) in place of the actual salinity profile. Using a linear regression to compare the predicted $\overline{\Theta}$ and $\overline{\Theta}_\mu$ ($r^2 = 0.97$, $\text{var}_\Theta = 0.1°\text{C}^2$), we can deduce that salinity variability would introduce an error in $\overline{\Theta}$ of up to 0.06°C. This value is smaller than the typical seasonal and summer interannual variability in $\overline{\Theta}$ (0.35°, 0.31°C), but is of similar magnitude to the observed spatial variability within a given summer of 0.07°C. Therefore, we conclude that the impact of salinity of travel time is limited and that the interannual and seasonal travel time variability in SF is largely attributable to variability in temperature.

c. *Interpreting acoustic travel time*

Variability in τ is driven by the properties and relative distribution of water masses, which influence $\overline{\Theta}$. For example, an increase in τ could be the result of an increased thickness of the cold PW layer or could be the result of the decrease in temperature within a given layer. With a basic understanding of glacial fjord circulation one can link τ variability with the variability of physically meaningful quantities. Here we summarize basic concepts of fjord circulation and subsequently use them for the interpretation of τ.

Measurements and models have shown that, in the summer, the circulation is driven in large part by the release of subglacial runoff (or subglacial discharge; Straneo et al. 2011; Sciascia et al. 2013; Carroll et al. 2015; Slater et al. 2018)—atmosphere-driven melting at the surface of the ice sheet released into the fjord at depth. This injection of fresh, buoyant water drives an upwelling plume that entrains ambient waters including submarine meltwater from the glacier. The resulting circulation is similar to an estuarine exchange flow with an inflowing lower layer of oceanic water and an outflowing upper layer of GMW (Motyka et al. 2003).

In the winter, SF is dominated by a fluctuating baroclinic circulation, called the shelf-driven circulation (Jackson et al. 2014; Harden et al. 2014; Sutherland et al. 2014; Jackson and Straneo 2016). This circulation is typically driven by downwelling-favorable alongshore winds, northeasterlies, which depress the pycnocline on the shelf and drive an inflow into the upper layer of the fjord. Eventually the fjord adjusts, the pycnocline relaxes and the velocity reverses. Since this circulation mode varies the height of the pycnocline, it can produce an identifiable signal in acoustic travel time.

We use past studies of SF to estimate the impact on travel time that we can expect from the dominant drivers of heat variability: the shelf-driven circulation and the variability of inflowing AW. While the shelf-driven circulation and AW variability can affect heat content through changes in both layer thickness and layer properties, we simulate the shelf-driven circulation through changes to layer thickness only and AW variability through changes to layer temperature only. The shelf-driven circulation is associated with pycnocline fluctuations that are about 50 m (Jackson and Straneo 2016; Jackson et al. 2018). Using temperature profiles collected from CTDs, we estimate a vertical displacement of the pycnocline by 50 m would produce a change of τ equivalent to 1.4 ms (see Fig. S1 in the online supplemental material). Similarly, we account

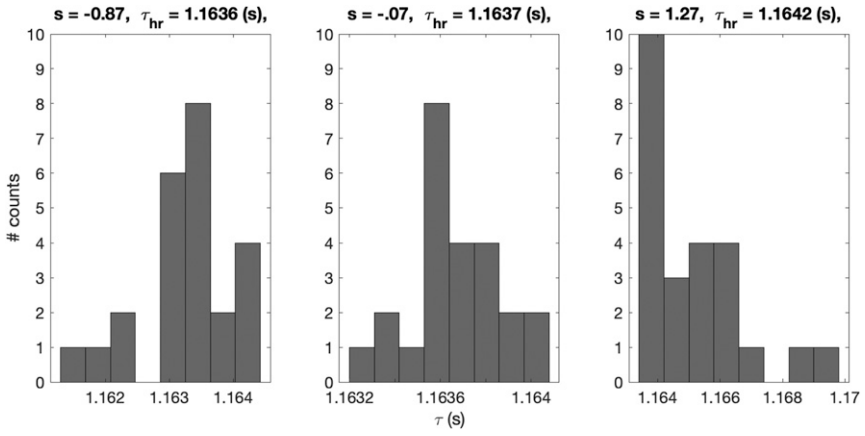

FIG. 4. Examples of the distribution of acoustic echoes received in an hour with the skewness (s) and averaged τ_{hr}. (a) A negatively skewed hourly distribution. (b) A weakly skewed hourly distribution. (c) A positively skewed hourly distribution (typical of the open ocean).

for the impact of AW temperature variability on τ by decreasing the AW layer temperature in a CTD cast by 0.1°C—the average standard deviation of temperature on synoptic (4–10 day) time scales. Decreasing the AW temperature by 0.1°C produces a change in τ of 0.3 ms. On interannual time scales, however, the inflowing AW temperature can vary by as much as 1°C (Straneo et al. 2016). Decreasing the AW temperature by 1°C produces a change in τ of 1.6 ms, which is roughly equivalent to the impact of pycnocline fluctuations. Therefore, inflowing AW variability produces a variability in τ comparable to the shelf-driven circulation over much longer time scales.

3. Data and processing

The PIES measures τ by releasing a 12 kHz acoustic ping and recording the echo from the sea surface. It sends a burst of 4 pings every 10 min and records the first 4 echoes from each burst for a total of 24 echoes an hour. To prevent nearby reflectors from dominating the signal, for example, overlying floats, the PIES incorporates a ''lockout time'' and only listens for returns after a set amount of time has elapsed. The ''lockout time,'' however, does not guarantee that the remaining echoes are from the surface. Other strong reflectors such as icebergs, sediments, and small organisms (e.g., Watts et al. 2006) can also lead to an early echo.

When icebergs pass over a PIES field of ''vision,'' they affect the travel time magnitude enabling an estimation of iceberg draft and speed (Andres et al. 2015; FitzMaurice et al. 2016). Additionally, the presence of sea ice can act as a rigid cap and reduce observed travel time variability (Andres et al. 2015; supplemental material, Fig. S4) Here, we filter out the ice-influenced signals and instead focus on times when the echo is from the sea surface and the travel time is informative of ocean heat content. Therefore, the first step in PIES processing is to remove those echoes that are from reflectors within the water column. In this case, we chose to remove echoes that were 0.007 s (approximately 10 m) less than the median travel time, $\tau = 1.1628$ s (supplemental material, Fig. S3). This cutoff value is generous enough to ensure that all potential surface data are retained while also removing those echoes that are obviously not from the sea surface. Among the discarded echoes are those used by Andres et al. (2015) to track icebergs.

After the initial filtering of the PIES returns, the remaining pings ($n < 24$) are averaged to produce a single-hourly travel time (τ_{hr}). In traditional PIES environments, sea surface scatter is the dominant source of noise, and the remaining pings produce an hourly distribution that is skewed toward late returns (Li et al. 2009). In general, if a distribution is positively (negatively) skewed it has a tail extending to the right (left) of the distribution. Under conventional PIES processing, the quartile method is used to generate an appropriate average of τ_{hr} (Kennelly et al. 2007). In the quartile method, pings are sorted by τ and the average of the first $n/6$ values past the first quartile are used to determine τ_{hr}. For example, if all pings made it past the first filter, then $n = 24$ and the average of the sixth through ninth quickest return echoes would determine τ_{hr}.

We found that in a glacial fjord, the return distribution of echoes was not consistently skewed. The presence of sea ice and smaller icebergs can influence the return signal and produce a bias toward early echoes (left skewed) rather than the late echoes typically seen in the open, ice-free ocean. Therefore, we modified the traditional quartile method to account for potential early echoes. First the skewness, or third-central moment, of the hourly distribution was calculated. If the skewness of the hourly distribution was greater than 0.5, the original quartile method was used (Fig. 4c). If the skewness was between −0.5 and 0.5, then the average of the $n/6$ values surrounding the median were used to determine τ_{hr} (Fig. 4b). If the skewness was less than −0.5, the average of the first $n/6$ values prior to the third quartile value was used to determine τ_{hr} (Fig. 4a).To ensure a large enough sample size to compute the skewness, hourly distributions with $n < 16$ were discarded. Roughly 20% of the τ_{hr} were removed because they did not meet this criterion. Gaps in the time series were filled through linear interpolation. Any large spikes in the data, such as those greater than three standard deviations from their nearest

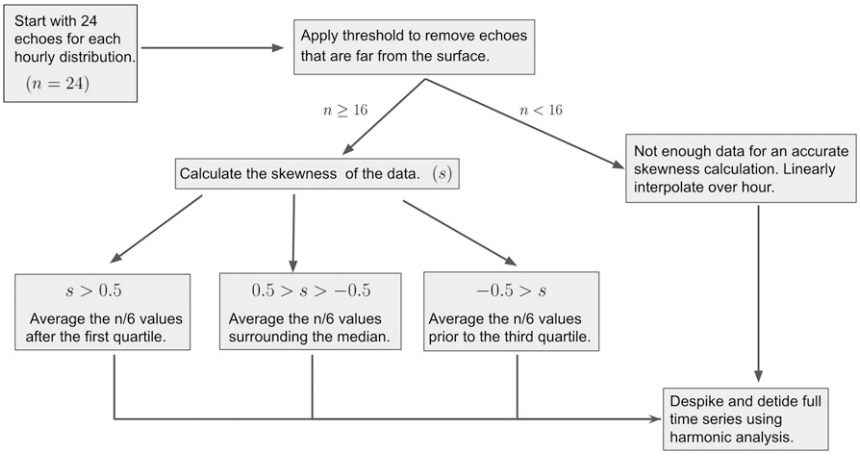

FIG. 5. A flowchart of the methodology used to process the PIES hourly return echoes.

neighbor, were removed. Last, the tidal fluctuations from the τ_{hr} signal were removed using harmonic analysis (Pawlowicz et al. 2002). A flowchart of the method for processing the PIES is given in Fig. 5.

The PIES also includes a pressure sensor that can be used to identify changes in the pathlength of the acoustic ping. After removing the atmospheric pressure (10.1325 dbar), the pressure record shows a mean bottom pressure of 862.55 dbar and tidal amplitudes of ±1.8 m during spring tides and ±0.5 m during neap tides (Andres et al. 2015). While the induced tidal velocities in the fjord are weak, the tides still contribute significant enough change in the water column depth to be seen in the travel time record due to their effect on the pathlength traveled by the acoustic pings. The pressure record was detided, and the residual pressure variations had an effect on travel time of about 10^{-4} s, an order of magnitude smaller than changes due to the water column heat content. Additional changes to the pathlength can occur through internal waves, which have a small expression in the sea surface, but these have a comparatively small effect and can be smoothed though low-pass filtering (Li et al. 2009). The pressure record is used here to get an accurate reading of the depth of the PIES and estimate the magnitude of travel time variations associated with tides but is not used otherwise.

The PIES was deployed alongside a mooring (M1, Fig. 1) equipped with CTDs and thermistors so that the travel time calculated from the directly measured hydrographic properties using the sound speed equation of Del Grosso (1974) could be compared with the PIES-measured acoustic travel time (Table 2; also Jackson et al. 2014; Jackson and Straneo 2016). The surface-most instrument on M1 was set to 246 m to limit damage from icebergs. A second set of shallower moorings (M2) was deployed in an embayment on the eastern side of the fjord with CTDs at 125 and 261 m. Like Jackson and Straneo (2016), we assume the cross-fjord differences between M1 and M2 are small and treat the moorings as if they are in the same location. This assumption is supported by CTD surveys, which reveal small lateral variability in water properties compared to the depth and time variability documented by the moorings. Additionally, comparisons of CTDs deployed around 250 m display a small difference (~0.3°C) compared to the instrument's overall temporal variability (0°–5°C). At 852 m depth, a CTD was mounted externally on the PIES and agreed with a calibrated PIES internal temperature sensor to within 0.01°C (Meinen et al. 2020). All vertical gaps in the mooring data were filled with linear interpolation. However, due to biofouling the conductivity data at the bottom were unusable and salinity was extrapolated to

TABLE 2. Details of mooring instrument setup. Platform location is specified in the map in Fig. 2.

Platform	Instrument	Measurement	Sampling period (min)	Depth (m)
M1	RBR XR-420 CTD	Conductivity, temperature, pressure	30, 30, 15	246, 657
	SBE37 MicroCAT CTD	Conductivity, temperature, pressure	7.5	396, 541
	Onset HOBO Tidbit v2	Temperature	30	276, 296, 316, 336, 356
	75kHz RDI Teledyne Workhorse Long-Ranger ADCP (upward facing)	Velocity	120	396 m to surface (10 m bins)
M2	SBE37 MicroCAT CTD	Conductivity, temperature, pressure	7.5	125, 261
P1	Pressure inverted echo sounder	Acoustic travel time, temperature, pressure	60, 7.5, 7.5	852
	SBE37 MicroCAT CTD	Conductivity, temperature, pressure	7.5, 7.5, 7.5	852

the seabed using conductivity measured at 657 m and the salinity gradient from deep CTD casts. Last, the mooring M1 was equipped with an upward-facing acoustic Doppler current profiler (ADCP; Table 2) that was analyzed in Jackson et al. (2014) and is used in this paper to provide a reference velocity (section 4b).

4. Results

a. *Estimating the thickness and temperature of inflowing AW in the winter*

Here we develop a model that relates variations in τ to simultaneous variations in the depth of the pycnocline, building on the results of Jackson and Straneo (2016), who showed that the fjord can be described as a two-layer system in the winter and that pycnocline displacement dominates the heat content variability within the fjord. A two-layer model is appropriate for SF in the winter because submarine melt is reduced and the PW and AW layers each remain weakly stratified. Additionally, since only two water masses dominate the fjord, the thermocline is at approximately the same depth as the halocline and the average temperature of the fjord can be estimated solely by knowing the depth of the pycnocline (Jackson and Straneo 2016).

Details of the two-layer model (2LM) are given in appendix A, but in short, the model assumes a two-layer structure for temperature and salinity and shifts the pycnocline depth to match the observed τ. The model takes as its input travel time $\tau(t)$ and bottom temperature $\Theta_{\text{bot}}(t)$ and gives as its output the vertical structure of temperature $\Theta_{\text{2LM}}(z, t)$ and pycnocline depth $z_{\text{pyc}}(t)$ (Fig. 6).

A comparison of the model and mooring observation record is given in Fig. 7 and visually the two appear similar during the time period (winter) when we expect the two-layer model to be valid. During this window, the root-mean-square deviation (RMSD) between temperature measurements at 550 and 852 m is 0.21°C, compared to the overall standard deviations of 0.48° and 0.41°C, respectively, showing that the typical vertical temperature difference is smaller than the temporal variability. Therefore, in this fjord, which lacks a shallow sill, we can use a bottom temperature sensor as a proxy for the temperature of the whole inflowing layer.

Quantitatively, we define the 2LM to be valid if it can predict the core AW temperature, the pycnocline depth and the ocean heat content within a level of error less than the observed variability. Here we define error as being the RMSD between the observed and 2LM estimated variable. We first consider the core AW temperature, which we define as the mean AW temperature between 450 and 650 m, we find that the 2LM estimate is correlated with observed core from the mooring AW temperature ($r^2 = 0.68$, $\text{var}_{\text{AW}} = 0.14°\text{C}^2$) with an error of 0.27°C compared to the observed standard deviation of 0.37°C. The correlation is improved by smoothing the data to monthly (>30 day) time scales through the use of a low-pass filter. On monthly time scales, we find a strong correlation ($r^2 = 0.78$, $\text{var}_{\text{AW}} = 0.13°\text{C}^2$) and the error is reduced to 0.23°C, which is smaller than both the observed monthly standard deviation of 0.36°C and previously published estimates of the AW interannual variability of 1°C (Straneo et al. 2016). Thus, the 2LM is successfully able to estimate the temperature of the core of the inflowing AW to within about 20% of the observed interannual variability.

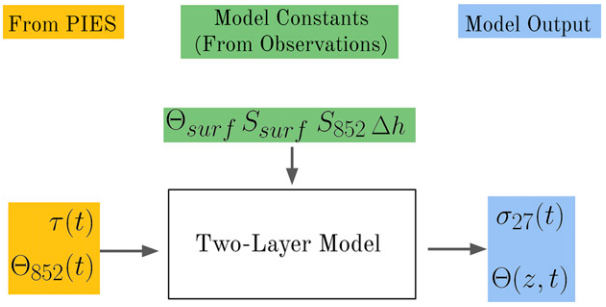

FIG. 6. Schematic showing how the PIES travel time data can be used to determine the temperature and thickness of the inflowing AW. The model takes as its input from the PIES: travel time (τ) and bottom temperature (Θ_{bot}). It gives as output the depth of the pycnocline (z_{pyc}) and estimated two-layer temperature (Θ_{2LM}). The model is tuned to Sermilik Fjord using constants derived from the XCTD observations: surface temperature (Θ_{surf}), surface salinity (S_{surf}), bottom salinity (S_{bot}), and pycnocline thickness (Δh) and is detailed in appendix A. The depth of the pycnocline is the depth of σ_{27}.

In addition to AW temperature, the 2LM predicts the depth of the pycnocline. The pycnocline, defined here as the isopycnal $\sigma = 1027\ \text{kg m}^{-3}$ is shown in black in the top panels of Fig. 7 and roughly tracks the interface between cold and warm waters in both the model and observations. This pycnocline is further examined in Fig. 7c, which compares the pycnocline depth from the mooring and the 2LM over the entire PIES record. The 2LM pycnocline is at a similar depth as the mooring pycnocline ($r^2 = 0.61$,$\text{var}_{\text{pyc}} = 1680\ \text{m}^2$) and only diverges in the spring when the stratification starts to reflect the arrival of GMW. The error between the 2LM pycnocline and the mooring pycnocline during the winter is 34 m, which is smaller than the observed pycnocline standard deviation of 41 m. On monthly time scales, the 2LM estimate is improved ($r^2 = 0.77$, $\text{var}_{\text{pyc}} = 978\ \text{m}^2$) and the error is reduced to 25 m, which is substantially smaller than both the observed monthly standard deviation of 35.5 m and the seasonal pycnocline depth range of about 200 m.

We can take the τ-derived 2LM output (temperature and pycnocline depth) to calculate the ocean heat content (OHC) of the AW layer. OHC is calculated with

$$\text{OHC}_{\text{AW}} = \rho c_p \int_{852}^{z_{\text{pyc}}} \Theta - \Theta_0 \, dz, \tag{2}$$

where ρ is density, c_p is the specific heat capacity, Θ_0 is the reference temperature, 852 is the depth of the PIES, and z_{pyc} is the depth of the pycnocline. We set $\Theta_0 = -2.6°\text{C}$, the freezing point of seawater for an Absolute Salinity of $35\ \text{g kg}^{-1}$. OHC, a function of both temperature and thickness, provides an estimate of the energy available for melting and is a variable that can be used to link heat from the North Atlantic with glacial retreat. OHC derived using τ and the 2LM is shown alongside the mooring-based calculation in Fig. 8. The OHC calculated

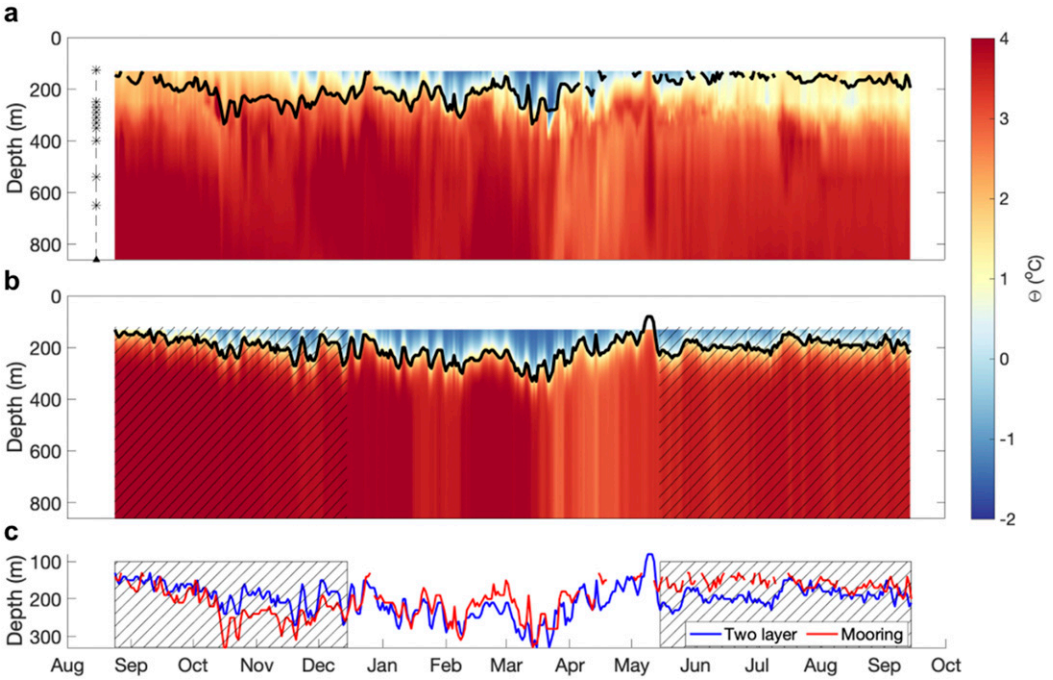

FIG. 7. (a) Conservative Temperature vs depth from mooring data (August 2011–October 2012) with the locations of the instruments noted and the isopycnal $\sigma_{27} = 1027\,\mathrm{kg\,m^{-3}}$ shown in black. Note that the shallowest instrument is located at 125 m. The tick marks on the horizontal axes of this and all subsequent time series denote the beginning of the month. (b) Conservative Temperature vs depth (m) created from the two-layer model of the fjord. Areas outside of the winter months are hatched and the visualization is limited to 125 m for easy comparison with the moored data. (c) Comparison of pycnocline depth represented by the isopycnal σ_{27} as derived from observations and from the model. Note that the mooring record is limited to 125 m, so it is impossible for it to capture the shallowest excursions of the pycnocline such as the peak in May.

from the moorings and 2LM are highly correlated ($r^2 = 0.82$, $\mathrm{var_{OHC}} = 1.7 \times 10^{14}\,\mathrm{J^2\,m^{-4}}$), and we find the 2LM can predict OHC (approximately $1.54 \times 10^{10}\,\mathrm{J\,m^{-2}}$) with an error of 3%, which is smaller than the observed standard deviation of 8% and seasonal range of 34%. The success of the 2LM in estimating OHC—a combination of pycnocline depth and AW temperature—demonstrates that the PIES can provide sufficiently accurate (on monthly time scales) long-term monitoring of fjord heat content during the winter, a time of year that is both challenging and expensive to collect in situ measurements.

b. *Monitoring the shelf-driven circulation*

The shelf-driven circulation in SF is responsible for rapidly transporting heat from the shelf toward the glacier and is the dominant mode of circulation outside of the summer (Straneo et al. 2010; Jackson and Straneo 2016; Fraser and Inall 2018). Monitoring of the circulation requires having temperature, salinity, and depth recorders in place to track the movement of the pycnocline induced by shelf–fjord exchange. However, as shown with the two-layer model, the position of the pycnocline is associated with a variability in travel time. In this section we examine the PIES's ability to monitor the synoptic variability of heat content associated with the shelf-driven circulation (Harden et al. 2014; Jackson et al. 2014).

First, we demonstrate that the PIES can observe a series of shelf-driven exchange events using those identified in Jackson et al. (2014). That study used this moored data including velocity data (M1/M2; Table 2) to identify the 16 strongest shelf-driven pulses through peaks in upper-layer volume flux. The upper layer was defined as being above the isopycnal $\sigma_{27} = 1027\,\mathrm{kg\,m^{-3}}$. An overlay of the upper-layer flux events are shown plotted on top of the travel-time record in blue and purple (Fig. 9a). The events coincide with sharp increases in travel time and indicate that the shelf–fjord exchange is recorded by the PIES. This hypothesis is further supported by a power spectrum of τ (Fig. 9b), which shows the dominant variability in travel time occurs on the time scales of the shelf-driven circulation (4–10 days).

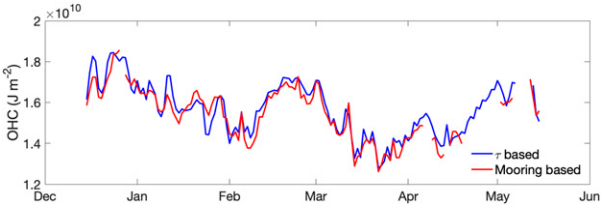

FIG. 8. OHC content of the AW layer, defined here as from 852 m to z_{pyc}, calculated from both the mooring data and τ.

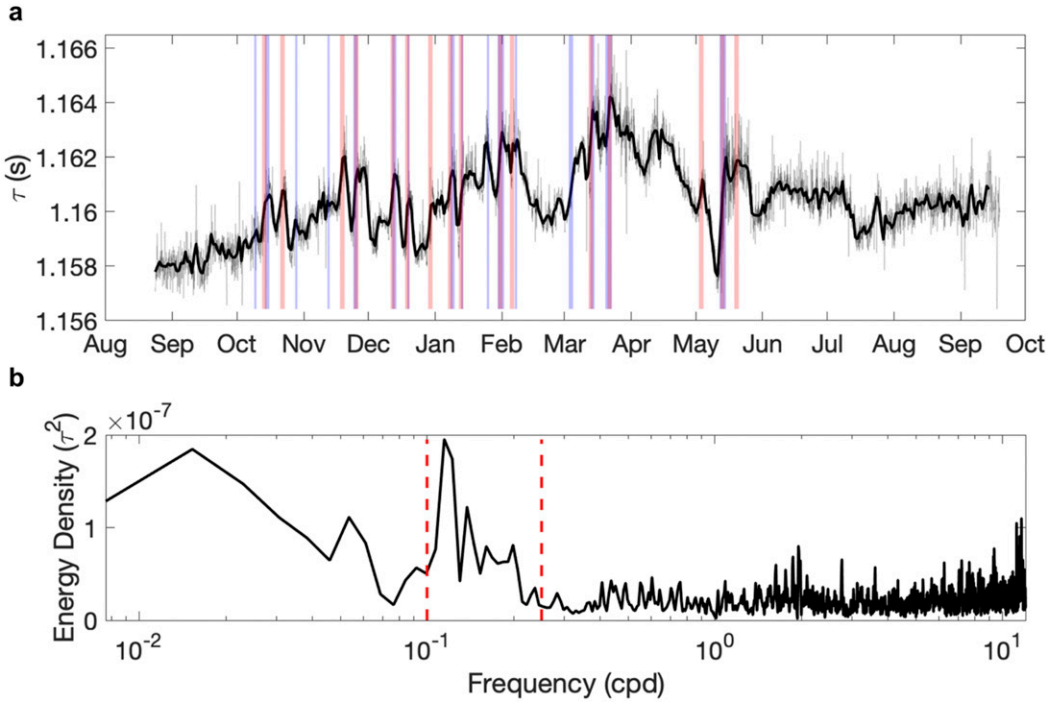

FIG. 9. (a) Travel time record from the PIES with the 16 largest shelf-driven exchange events from Jackson et al. (2014) overlain in blue. The shelf-driven exchange events defined using τ are overlain in red (see text for detail), with overlapping events in purple. (b) Variance-preserving power spectrum of the acoustic travel time time series in (a) with frequency given in cycles per day (cpd) and the 4–10 day period represented by the red dashed lines.

We define the PIES's ability to monitor the shelf-driven circulation a success if through the use of τ it can predict maximum pycnocline height and peak velocity with a prediction error and uncertainty less than the observed uncertainty. Uncertainty is defined here as the standard error. Significant variability exists from event to event and so we produce composites of all the events to reduce the error in the analysis. However, the RMSD calculated from all the individual events is also presented.

We start with two time series: τ_{hr} and depth of the pycnocline calculated from the moored record (z_{pyc}). The time series are bandpass filtered to keep signals between 26 h and 30 days. This filtered version of τ_{hr} we define as τ_f. Composites are generated by averaging around the peak volume flux events identified from Jackson et al. 2014 (Fig. 9a, blue and purple). At the peak volume flux, the composite has increased about 1.5 ms from 50 h earlier, equivalent to a depth change of about 50 m (Fig. 10). The increase in τ_f is due to a thickening of the PW layer as the pulse moves into the fjord. The thicker PW layer results in a colder average temperature and a slower travel time. Around 4 days after the event, τ_f returns to normal, but the events often follow one another resulting in a forcing frequency between 4 and 10 days. After fitting a linear regression between τ_f and z_{pyc} (not shown), we can estimate the magnitude of the pycnocline fluctuation from τ_f (dashed line, Fig. 10). The predicted maximum pycnocline height has a prediction error of 3.9 ± 6 m, which is smaller than the composite z_{pyc} uncertainty of 8 m (Fig. 10, red shading). Examining the shape of the composite, there is a notable lag of about 34 h between the second peak in τ_f and the peak volume flux ($t = 0$). We find the second peak is anticorrelated with pycnocline temperature ($r^2 = 0.6$, $\text{var}_{\text{pyc}-\Theta} = 0.02°\text{C}^2$; supplemental material, Fig. S5) and is potentially linked to the arrival of new

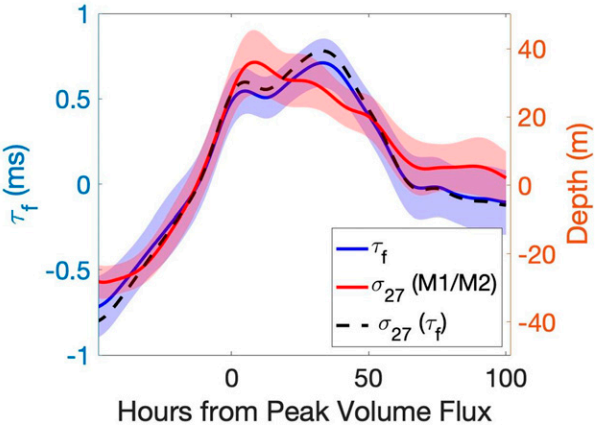

FIG. 10. Composites of τ_f (blue, left axis), isopycnal σ_{27} (red solid, right axis), and isopycnal σ_{27} predicted from τ_f (dashed, right axis) centered around the peak volume flux (Fig. 9a, blue shading). Note that isopycnal depth is flipped upside down so that it can be easily compared with travel time. All composites are of data that have been 26 h low-pass filtered with the 30 day low-pass filter background removed. The uncertainty is the standard error of the composite.

waters from the shelf. However, we do not find a consistent phasing for this second peak and it has a large standard deviation of 17 h. We conclude that τ_f has a broader peak in response to shelf forcing than pycnocline depth because it is responding to both changes in layer thickness and water properties. Next, we evaluate the relationship between z_{pyc} and the pycnocline height predicted by τ_f for the individual events. The RMSD calculated from the individual events is 28 m, which is substantially higher than the composite error but is comparable to the observed standard deviation of maximum pycnocline amplitude of 31 m. This mismatch highlights the ability of the composite to provide a clearer picture of the relationship between τ_f and z_{pyc}. In short, τ can be used to estimate the average magnitude of pycnocline fluctuations associated with the shelf-driven exchange with an error of 50% of the observed standard error.

Knowing the magnitude of the pycnocline fluctuations, we can also make an estimate of the shelf-induced velocity within the fjord. Recent work has shown that the pulses associated with the shelf-driven circulation can be described as a combination of standing and Kelvin waves (Jackson et al. 2018). Specifically, the average velocity of the upper layer of the fjord can be estimated from Eq. (29) of Jackson et al. (2018), with details of the calculation provided in appendix C. Using the estimated pycnocline depth from the PIES, the equation predicts a peak velocity and standard error of $0.41 \pm 0.03\ \mathrm{m\,s^{-1}}$. For comparison, the recorded peak velocity from an ADCP in the upper layer is $0.43 \pm 0.05\ \mathrm{m\,s^{-1}}$. However, the RMSD of predicting the peak velocity from individual events is $0.22\ \mathrm{m\,s^{-1}}$, which is slightly larger than the observed standard deviation of peak velocity of $0.18\ \mathrm{m\,s^{-1}}$.Therefore, the PIES appear better suited to monitor the average peak velocity from shelf-driven events rather the velocity of individual events.

We can combine the composite approach with the 2LM to estimate the average heat flux associated with the shelf-driven circulation. First, we calculate the upper-layer OHC using the 2LM output and a modified form of Eq. (2) and then subtract a low-pass (30 day) background signal—the same approach used to generate the τ_f composites. After averaging across the 10 shelf-driven events that occurred between December and May and multiplying by fjord width (7.5 km) and predicted average peak velocity ($0.41 \pm 0.03\ \mathrm{m\,s^{-1}}$), we calculate an average heat flux of $7.0 \pm 1.8 \times 10^{11}$ W for each shelf-driven exchange. The uncertainty in the heat flux estimate includes both the standard error and the propagated uncertainties from the peak velocity and OHC estimates. To put this heat flux into context, Jackson et al. 2016 calculated a heat budget of Sermilik Fjord and estimated that the average winter heat flux associated with the storage term was $0.3 \pm 7.5 \times 10^{10}$ W. Therefore, the shelf-driven events potentially bring a heat flux an order of magnitude higher than the background storage rate and can substantially increase the heat content of the fjord.

We have demonstrated that the shelf-driven circulation excites a response in travel time that can be measured and used by the PIES. Through the use of composites the variability in the τ_f signal can be reduced and sufficiently accurate predictions can be made of average maximum pycnocline amplitude and average peak velocity. However, for effective long-term monitoring the PIES needs to be able to demonstrate the ability to measure these events without the use of an ADCP. Therefore, we develop our own criteria for finding shelf-exchange events and define events as a peak in τ_f that is greater than 0.95 ms. The events identified through τ_f are plotted alongside the Jackson et al. 2014 events in red, with events identified by both criteria in purple. Our definition of events coincide for the majority of pulses and primarily mismatches when the peak volume flux is not associated with a large pycnocline fluctuation and thus a peak in τ_f (Fig. 9a, blue). These new events can be averaged to produce a composite of τ_f that is centered on 34 h prior to the peak in τ_f to account for the previously discussed phase shift between τ_f and peak volume flux. A new estimate of maximum pycnocline amplitude derived from peaks in τ_f had a composite prediction error of 3.7 ± 5.6 m, which is similar to the error 3.9 ± 6 m, which was found using the actual shelf-driven exchange events. The precision of detection could likely be improved by correlating alongshore wind stress with peaks in τ (Jackson et al. 2014), but our demonstration was focused on what monitoring could achieve with the use of a PIES alone. We conclude that through appropriate averaging a PIES achieves our criteria for successfully monitoring the frequency, magnitude, and peak velocity of shelf-driven exchange events.

c. *Measuring the heat content of the top layer*

1) CONVERTING τ TO τ_{top}

Moored instruments in glacial fjords often have a limited vertical range because of the potential damage from icebergs. For example, in this mooring dataset, the shallowest CTD was deployed at 125 m, which is below the bulk of outflowing GMW (Beaird et al. 2018). Here, we show how PIES can be utilized, in combination with subsurface moorings, to measure the portion of water column that cannot be sampled by moored instrumentation. We define this unsampled region, which spans 0–125 m, as the top layer, and it should not be confused with the area above the pycnocline, which was referred to earlier as the upper layer.

Given a subsurface property record from a mooring and a full-depth τ record, we combine these to derive the travel time of the top layer. In this case

$$\tau_{\mathrm{top}} = \tau - \tau_{\mathrm{Mooring}}, \tag{3}$$

where τ_{top} is the travel time from 0 to 125 m, τ is the PIES recorded travel time (0–852 m), and τ_{Mooring} is the travel time calculated from sound speed (1) using the moored instruments (125–852 m).

As a check that the residual τ_{top} is within expected values, τ_{top} was compared against travel times of the upper 125 m calculated from CTDs. The mean 125 m travel time calculated for the summer (1 July–30 September) was $\tau_{\mathrm{topS}} = 0.1727 \pm 0.0004$ s and for the winter (1 January–1 April) was $\tau_{\mathrm{topW}} = 0.1738 \pm 0.0005$ s. The average travel time calculated from the CTDs over these time periods was $\tau_{\mathrm{CTDS}} = 0.1727 \pm 0.0003$ s for the summer and $\tau_{\mathrm{CTDW}} = 0.1739 \pm 0.0002$ s for the winter. Given an uncertainty estimate of 0.0004 s (appendix B), this

supports that the residual τ_{top} is a valid representation of the travel time of the upper 125 m.

Since travel time and mean temperature are proportional (section 2), we can use the relationship

$$\overline{\Theta}_{top} = A\tau_{top} + B, \quad (4)$$

to calculate the mean temperature of the upper 125 m ($\overline{\Theta}_{top}$) where the constants A and B are determined from a linear fit of hydrography (Fig. 3b). The average temperature of the upper 125 m generated with τ_{top} is shown in Fig. 11. The linear fit occasionally produced values below freezing. Therefore, we cap the average temperature at the freezing point, $\Theta_f = -1.9$°C, calculated using a pressure of 125 dbar and an Absolute Salinity of 33.1 g kg^{-1}.

The time series was smoothed using a 10 day low-pass filter and shows the general progression of the average temperature from warmer in the summer to colder in the winter. Starting in late March, the time series shows a general warming trend, which, based on pycnocline depth (Fig. 7), is associated with a thickening of the AW layer. While there are no contemporaneous temperature data available to compare against the residual calculation, a CTD recorded temperature at 60 m from September 2012 to August 2013 (see Jackson and Straneo 2016). The 30 day low-pass filtered 60 m Conservative Temperature is shown compared to the 125 m average temperature in Fig. 11. While there are obvious differences between the two signals arising from interannual variability and the fact that the τ-based signal is an average temperature over 125 m while the observed signal is the temperature at just 60 m, they exhibit a comparable magnitude (4°C) and both show falling temperatures from October to December and rising temperatures in July. While this comparison cannot be used to validate the τ_{125} approach it is reassuring that the seasonal signals are qualitatively similar.

2) Identification of extreme temperature events

Katabatic winds, or piteraqs, are common in southeast Greenland and are capable of influencing fjord properties and inducing an exchange flow similar to alongshore winds (Oltmanns et al. 2015; Spall et al. 2017). However, the influence of piteraqs on fjord properties is still poorly understood because the effects are primarily felt in the surface layer of the fjord. The strong down-fjord winds depress the pycnocline and therefore are associated with a signal in τ. Here we demonstrate that with the PIES remotely measuring the top-layer heat content, we can observe the impact of extreme events, such as piteraqs, on fjord temperatures.

A piteraq occurred in SF in May 2012 and is associated with a large temperature drop in $\overline{\Theta}_{top}$ (Fig. 11) and a shelf-driven exchange event in the τ record (Fig. 9). Focusing in on the event that appears to start on 9 May, the average temperature of the upper 125 m drops by nearly 2°C to hover around the freezing point (Fig. 12a). Satellite imagery from NASA MODIS shows the fjord initially with low ice cover (Fig. 12b), then abruptly covered with sea ice (Figs. 12c–e), then the ice flushed out of the fjord (Fig. 12f). We are confident the signal is a result of changing temperature rather than contamination by sea ice because ice influence would result in a shorter observed travel time and therefore an increase in temperature. However, further investigation of the piteraq is outside the scope of this paper and a PIES-based piteraq analysis would also need to incorporate local wind data to differentiate shelf-driven events from piteraqs.

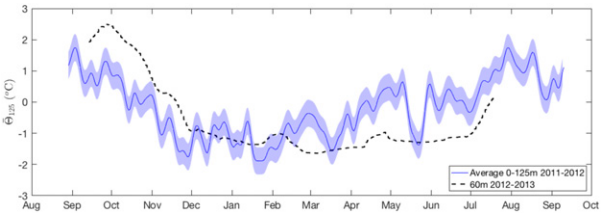

FIG. 11. The average temperature of the upper 125 m, generated from a residual travel time with a 10 day low-pass filter and uncertainty given in lighter shading. The large drop in May is one of the events identified in Fig. 9 and is due to a piteraq. For comparison, the dashed line is Conservative Temperature recorded at 60 m from September 2012 to August 2013 (see Jackson and Straneo 2016).

5. Discussion

a. *Estimating the thickness of AW in the summer*

The two-layer model demonstrates that with background knowledge of fjord stratification, travel time can be used to effectively monitor the thickness and properties of inflowing AW in the winter. However, estimating the thickness of the AW layer in the summer is significantly more difficult due to the release of subglacial runoff and the formation of GMW. GMW is composed primarily (88%; Beaird et al. 2018) of entrained and upwelled AW, and appears as a warm, salty intrusion in the upper layer of the fjord. Therefore, the total water column heat content is a function of both the thickness of the AW layer and the GMW concentration in the summer.

A simple model to predict the vertical temperature structure in the summer has proved elusive. As the GMW reaches its neutral buoyancy it can mix and increase fjord stratification breaking down the two-layer system. The neutral buoyancy depth of GMW is a function of subglacial runoff flux, fjord stratification and AW temperature (Carroll et al. 2016; Slater et al. 2016; De Andrés et al. 2020), making prediction from τ alone with the present data nearly impossible. Future work with PIES and the development of theory will be necessary before τ can measure both the extent of thermal forcing in the summer and the export of GMW. For now, these competing signals limit the PIES to measuring only the bottom temperature during the summer.

b. *Determining the bounds for the two-layer model*

We believe that the two-layer stratification breaks down with the arrival of significant amounts of subglacial discharge in the summer and this can be observed in Fig. 11 as the temperature rises in July. However, the transition between summer and winter and how long GMW resides in the fjord in the

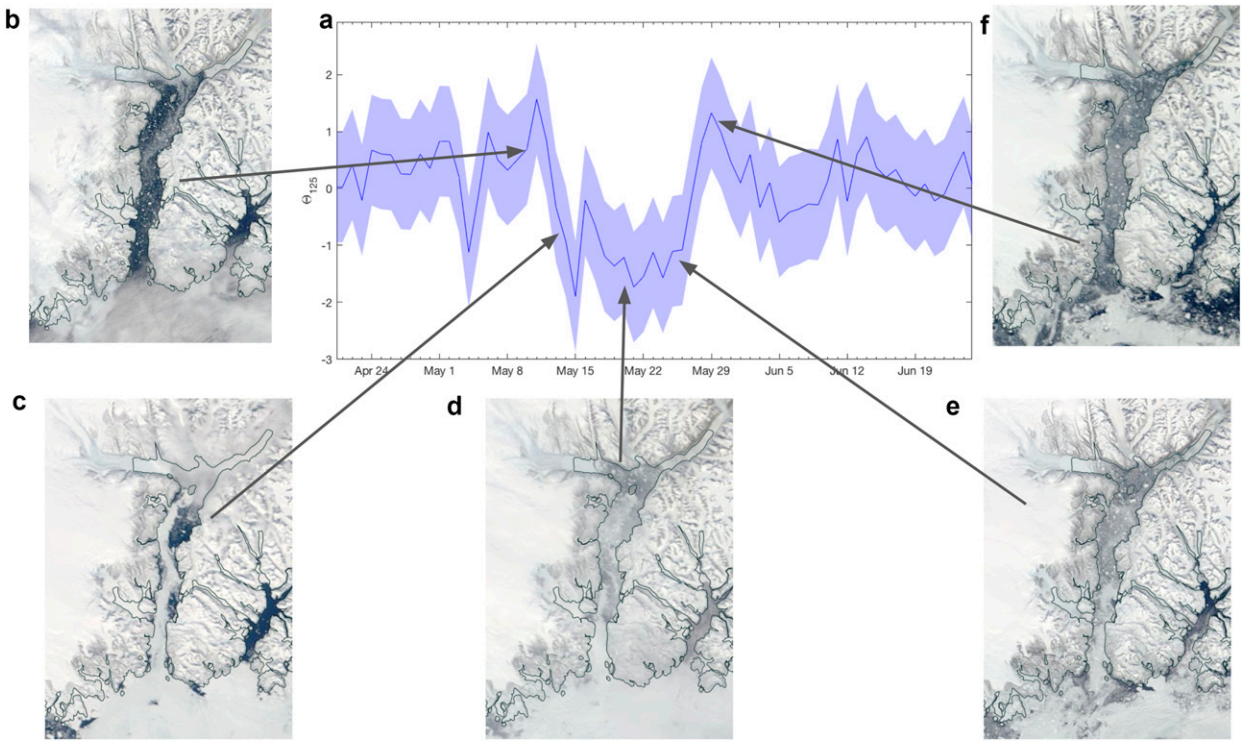

FIG. 12. (a) Zoom in on the piteraq event and the corresponding drop in average temperature in the upper 125 m of the fjord. (b)–(f) MODIS images showing the sea ice coverage of the fjord from the days of 10, 13, 20, 26, and 29 May 2012.

fall is an open question and the topic of current research. With travel time alone, it is difficult to distinguish if warm water observed in the fall is a remnant of GMW or a seasonal intrusion of warm water originating from the shelf. However, the few CTD casts collected in winter (March) near the location of the PIES show only a weak signal of melting indicating that fjord properties are likely being more influenced by the shelf stratification than the glacier at this time of year. Additionally, the shelf-driven baroclinic circulation is clearly active by October (Jackson and Straneo 2016) enabling rapid communication between the shelf and the fjord and potentially aiding in the flushing of GMW out of the fjord. Jackson et al. (2014) found that the average volume exchanged with each shelf-driven event was equivalent to 50% of the total upper-layer volume. Therefore, it might be that case that the fjord becomes ''two layer'' when the adjacent shelf is two layer rather than when all the GMW has been removed from the fjord. For the purposes of monitoring the heat content of fjords we have chosen to define the winter when the two-layer model is successful (December–May) and emphasize the usefulness in the overlapping of PIES and moored data for over a year so that this window can be determined for each individual fjord system.

c. *Deployment considerations*

A PIES can be deployed in glacial fjords that get covered in sea ice. While sea ice results in a reduced variability of travel time pings due to the reduction of sea surface scatter (see Andres et al. 2015) we can still extract a coherent travel time signal in the presence of sea ice since it is a strong reflector at the sea surface. For example, SF was covered in landfast ice for about two weeks from 26 February to 10 March 2012, but we do not have a gap in our travel time series. Our method of averaging hourly travel time is designed specifically to account for the potential changes to travel time due to the presence of sea ice. Sea ice with a thickness of 1 m would potentially decrease travel time by 0.7 ms (comparable to a thermocline shift of 27 m), but this effect is offset by the cooling of ocean temperatures during sea ice formation (supplemental material, Fig. S4).

Careful consideration should be given to the location of PIES deployment within glacial fjords. A significant challenge of operating a PIES around ice is extracting signal from areas with semicontinuous iceberg coverage as the majority of pings will be off of icebergs rather than the surface. Specifically, we think that regions that have a high concentration of ice coverage with heterogeneous and deep drafts (deeper than several meters), such as a near-terminus mélange, can prevent the PIES from recording a surface measurement. While this might be addressed by limiting the PIES listening range (the ''lockout time'') to the expected travel time of echoes coming from the surface, it is possible that the echoes would never come in a large enough signal to detect. In SF, we found this to be the case for a PIES deployed about 30 km from the terminus. However, the PIES located around 70 km from the terminus had enough pings bounce off of the surface to produce a reliable travel time signal.

The PIES's effectiveness is also influenced by the choice of lockout time. In our second campaign of data collection, we

shortened the lockout time to be able to record more information about the depth of icebergs passing over the PIES. While this change improved the suitability of the record for iceberg detection, it limited the number of echo returns recorded from the sea surface since only the earliest echoes are recorded and we were not able to interpret the surface travel time signal. Thus, there are clear trade-offs when deciding between using the PIES to monitor icebergs or fjord heat variability.

When deploying the PIES in a glacial fjord, it is recommended that for the first year the PIES is deployed alongside a traditional mooring. The PIES can be utilized best when the basic dynamics of the studied fjord are understood and having a mooring present will enable an interpretation of temperature variability on τ. The PIES can then be used for long-term (5 years) monitoring of the fjord and prediction of heat content based on empirical relationships calculated from the first-year data.

d. *Applicability to other glacial fjords*

We have presented a case study on the use of acoustic travel time for a single glacial fjord, but the results and techniques are also applicable to some of Greenland's other fjords. While varying in size, Greenland's fjords share common features such as the presence of PW and AW, and a buoyancy-driven circulation in the summer (e.g., Mortensen et al. 2014; Gladish et al. 2015; Lindeman et al. 2020). Consequently, in the winter when melt rates are low, the fjords are likely to match the stratification on the shelf with cold PW overlaying warm AW (Straneo et al. 2012). Thus, the two-layer model is likely applicable to other fjord systems and could be changed to solve for parameters such as pycnocline thickness or upper-layer temperature. Even the failure of the model can provide insight into the dynamics and stratification of the fjord as it does in the case of SF in the summer. PIES would not be appropriate for glacial fjords that produce continuous mélange that extends out to the fjord mouth such as Ilulissat Icefjord, but PIES can work under sea ice or be deployed in the deep tributaries of major glacial fjords. Besides SF, examples of locations for potential PIES deployment include Nuup Kangerlua (Godthåbsfjord), Ikerasak Fjord (Store), Karrat Fjord (Rink), and Kangerdlugssuaq Fjord.

6. Conclusions

Understanding the heat variability of fjords is crucial to representing the forcing they apply to glaciers. However, glacial fjords are a challenging environment to observe due to the presence of icebergs and sea ice. We present the use of PIES in a glacial fjord to track heat content variability and monitor fjord circulation. While additional steps need to be taken to ensure the acoustic signal is not contaminated by ice, we have shown that PIES can be used in a glacial setting to measure vertically integrated heat content of the full water column. While the PIES should be combined with other platforms such as CTDs and moorings to make full use of their capabilities, they can also serve alone to recreate the vertical properties of the fjord in the winter. A single PIES can capture large wind events in SF, and without the use of an ADCP infer when pulses entered into the fjord. We envision PIES playing a role in an integrated system of monitoring glacial fjords due to their low-cost, reliability, and long-term measuring capability.

Acknowledgments. We would like to acknowledge Jamie Holte, Isabella Le Bras, and Margaret Lindeman for helpful discussion and suggestions. Dave Sutherland and Will Ostrom were crucial to the deployment and recovery of the PIES. We also acknowledge the support of the crew of the M/V *Viking*, Greenland, in carrying out the fieldwork. FS and MA acknowledge funding from the Kerr Family Foundation and the Grossman Family Foundation through the Woods Hole Oceanographic Institution. MA is supported by a grant from the National Science Foundation Office of Polar Programs (1332911). FS and RS acknowledge support from NSF OCE-1657601 and from the Heising-Simons Foundation. We also thank Michael Wood and two anonymous reviewers who substantially helped improve the manuscript.

Data availability statement. Data are available through the NSF Arctic Data Center at the following DOIs: PIES: doi:10.18739/A2RJ6S; bottom moored CTD August 2011–September 2012: doi:10.18739/A23X83M74; CTD profiles March 2010: doi:10.18739/A2M03XZ2K; CTD profiles August 2011: doi:10.18739/A2QN5ZC52; CTD profiles September 2012: doi:10.18739/A2VD6P58Q; CTD profiles August 2013: doi:10.18739/A2057CT39; CTD profiles August 2017: doi:10.18739/A2NG4GS8C. CTD data collected in 2015 were made available in the previously published work (Beaird et al. 2018). The remaining mooring data are available through the NOAA National Centers for Environmental Information (NCEI) using NCEI Accession Numbers 0126772 and 0127325.

APPENDIX A

Two-Layer Model of Sermilik Fjord

The 2LM assumes the vertical temperature profile of the fjord can be described by the equation

$$T_{2LM}(z) = A \tanh\left(\frac{z - z_{pyc}}{\Delta h}\right) + B, \tag{A1}$$

where z_{pyc} represents the depth of the pycnocline, Δh the thickness of the pycnocline, with A and B chosen so that the profile asymptotes to the boundary conditions of surface temperature (T_{surf}) and bottom temperature (T_{bot}). Specifically,

$$A = \frac{T_{bot} - T_{surf}}{2}, \tag{A2}$$

$$B = A + T_{surf}. \tag{A3}$$

Salinity is described by a similar equation and an assumption is made that temperature and salinity are tightly correlated and therefore sharing the same z_{pyc} and Δh.

The model assumes a constant Δh, T_{surf}, and S_{surf}. While the mooring observations indicate the depth of the pycnocline can fluctuate over a 100 m range, the relative thickness of the

interface remains constant until the arrival of GMW in the summer. Surface fluxes drive variation in T_{surf} and S_{surf}, but based on the winter survey the surface layer does not penetrate deep (~15 m), and solar insolation is generally weak in the winter justifying the constant T_{surf} and S_{surf}. Based on the XCTD casts, the constants were determined to be $\Delta h = 70$ m, $T_{surf} = -1.5$°C and $S_{surf} = 32.8\,g\,kg^{-1}$. The model was not sensitive to the choice of Δh, T_{surf}, or S_{surf}. However, the isopycnal chosen to represent the pycnocline is sensitive to the choice of surface salinity, and $S_{surf} = 32.8\,g\,kg^{-1}$ was found to best match the observations and is representative of PW surface salinity from the March 2010 survey. Since the winter casts we used to determine S_{surf}, and σ_{pyc} were collected in 2010 and the 2LM is evaluated on data from 2012 to 2013, this suggests the constants have some time invariance over multiple years. However, there might be decadal trends in surface salinity that the 2LM cannot account for and the constants may need to be periodically adjusted. T_{bot} was taken from the PIES, and S_{bot} was assumed a constant $34.75\,g\,kg^{-1}$. By taking T_{bot} from the PIES, the 2LM is able to adjust to background changes in the temperature of the AW layer. The value of S_{bot} has a minor effect on τ (section 2b) but could be improved by incorporating the salinity value from the CTD attached to the PIES. The model solves for z_{pyc} by generating a travel time from the 2LM (τ_{2LM}) and minimizing the difference between τ_{2LM} and the observed τ_{852}.

APPENDIX B

Error and Uncertainty

The uncertainty in the value of the τ_{hr}, derived from the spread of the return echoes, was estimated using the standard error approach. The standard error of the mean is given by

$$\delta = \frac{\sigma}{\sqrt{N}}, \tag{B1}$$

where σ is the standard deviation and N is the number of observations. δ_{hr} was found to vary from 0.01 to 0.4 ms, and so 0.4 ms was used in error propagation. The standard error was reduced to 0.1 ms by taking a daily mean of τ_{hr} and assuming an average of 19.2 (80%, section 3) valid hourly samples in a day.

The uncertainty in the conversion of the mooring profile into a pseudo–travel time was first estimated by computing a standard error of the daily mean for each of the instruments (see Table 2). Additional error (δ_{Loc}) was introduced by combining two mooring profiles in different locations. This error was estimated by computing the difference and standard deviation of two instruments both located around 250 m on M1 and M2. δ_{Loc} was added to the 125 m instrument standard error to account for its different location.

A Monte Carlo method was used to estimate the total uncertainty in the mooring generated pseudo–travel time. First, travel time was calculated for 23 CTD casts. For each of the casts another travel time was calculated using only the depths where instruments were located and with Gaussian noise equal to each instrument's standard error added. The uncertainty was estimated to be $\delta_{hr} = 0.4$ ms by taking the standard deviation of the difference between the actual and noisy travel times.

The uncertainty in the conversion of travel time to heat content was estimated by adding the RMSD of the linear fit to the propagated uncertainty of travel time. In other words, if

$$\hat{\Theta} = A\tau + B \tag{B2}$$

is the equation of the linear fit, then uncertainty exists due to both the linear fit and the uncertainty of τ. Defining this uncertainty as $\delta_\Theta = \text{RMSD} + A\delta_\tau$, where A is slope of the linear fit, the potential uncertainty is estimated as $\delta_\Theta = 0.82$°C. After a 10 day low-pass filter, the uncertainty was reduced to 0.39°C.

APPENDIX C

Calculating Velocity from Pycnocline Depth

The average velocity of the upper layer of the fjord can be estimated from Eq. (29) of Jackson et al. (2018):

$$\bar{v} = \Delta\sigma e^{-W/R_d}\underbrace{\frac{c_1}{h_1}\frac{\cos[\omega/c_1(L-y)]}{\cos(\omega L/c_1)}}_{\text{Standing wave}} + \Delta\sigma(1-e^{-W/R_d})\underbrace{2\frac{c_1}{h_1}\frac{R_d}{W}(1-e^{-W/R_d})\sin[\omega/c_1(L+W/2-y)]}_{\text{Kelvin wave}}, \tag{C1}$$

where the first term is the contribution from the standing wave and the second term is the contribution from the Kelvin wave. Here $\Delta\sigma$ is the range of pycnocline fluctuation calculated from τ_f, W is the fjord width, R_d is the deformation radius, c_1 is the baroclinic wave speed, h_1 is the depth of the upper layer, ω is the forcing frequency, L is the fjord length, and y is the location of the mooring. The Kelvin number,

$$\text{Ke} = \frac{W}{R_d},$$

TABLE C1. Parameters used in the wave velocity equation, Eq. (C1), to estimate velocity within the fjord. All values were derived or calculated from data within this paper and are consistent with the values used in Jackson et al. (2018).

Model constant	Sermilik Fjord value
Fjord width W	7.5 km
Deformation radius R_d	7.5 km
First baroclinic wave speed c_1	1.1 m s^{-1}
Depth of the upper layer h_1	200 m
Forcing period $1/\omega$	6 days
Fjord length L	90 km
Mooring distance from mouth y	30 km

can be used to scale the influence of rotation. As described by Jackson et al. (2018), interfacial waves in narrow fjords with a small Ke can be described using the 2D standing wave model. While interfacial waves in a wide fjord with a large Ke propagate as Kelvin waves. Like many of Greenland's fjords, SF has a Ke that is $O(1)$ and experiences both of these wave phenomena (Jackson et al. 2018). To estimate velocity using (C1), we use τ_f to predict $\Delta\sigma$, and appropriate values for SF for the remaining constants (Table C1).

REFERENCES

Andres, M., A. Silvano, F. Straneo, and D. R. Watts, 2015: Icebergs and sea ice detected with inverted echo sounders. *J. Atmos. Oceanic Technol.*, **32**, 1042–1057, https://doi.org/10.1175/JTECH-D-14-00161.1.

Bamber, J. L., M. Oppenheimer, R. E. Kopp, W. P. Aspinall, and R. M. Cooke, 2019: Ice sheet contributions to future sea-level rise from structured expert judgment. *Proc. Natl. Acad. Sci.*, **116**, 11 195–11 200, https://doi.org/10.1073/pnas.1817205116.

Beaird, N., F. Straneo, and W. Jenkins, 2018: Export of strongly diluted Greenland meltwater from a major glacial fjord. *Geophys. Res. Lett.*, **45**, 4163–4170, https://doi.org/10.1029/2018GL077000.

Boone, W., and Coauthors, 2018: Coastal freshening prevents fjord bottom water renewal in northeast Greenland: A mooring study from 2003 to 2015. *Geophys. Res. Lett.*, **45**, 2726–2733, https://doi.org/10.1002/2017GL076591.

Cape, M. R., F. Straneo, N. Beaird, R. M. Bundy, and M. A. Charette, 2019: Nutrient release to oceans from buoyancy-driven upwelling at Greenland tidewater glaciers. *Nat. Geosci.*, **12**, 34–39, https://doi.org/10.1038/s41561-018-0268-4.

Carroll, D., D. A. Sutherland, E. L. Shroyer, J. D. Nash, G. A. Catania, and L. A. Stearns, 2015: Modeling turbulent subglacial meltwater plumes: Implications for fjord-scale buoyancy-driven circulation. *J. Phys. Oceanogr.*, **45**, 2169–2185, https://doi.org/10.1175/JPO-D-15-0033.1.

——, and Coauthors, 2016: The impact of glacier geometry on meltwater plume structure and submarine melt in Greenland fjords. *Geophys. Res. Lett.*, **43**, 9739–9748, https://doi.org/10.1002/2016GL070170.

——, and Coauthors, 2018: Subannual and seasonal variability of Atlantic-origin waters in two adjacent west Greenland fjords. *J. Geophys. Res. Oceans*, **123**, 6670–6687, https://doi.org/10.1029/2018JC014278.

De Andrés, E. D., D. A. Slater, F. Straneo, J. Otero, S. Das, and F. Navarro, 2020: Surface emergence of glacial plumes determined by fjord stratification. *Cryosphere*, **14**, 1951–1969, https://doi.org/10.5194/tc-14-1951-2020.

Del Grosso, V. A., 1974: New equation for the speed of sound in natural waters (with comparisons to other equations). *J. Acoust. Soc. Amer.*, **56**, 1084–1091, https://doi.org/10.1121/1.1903388.

FitzMaurice, A., F. Straneo, C. Cenedese, and M. Andres, 2016: Effect of a sheared flow on iceberg motion and melting. *Geophys. Res. Lett.*, **43**, 12 520–12 527, https://doi.org/10.1002/2016GL071602.

Fraser, N. J., and M. E. Inall, 2018: Influence of barrier wind forcing on heat delivery toward the Greenland Ice Sheet. *J. Geophys. Res. Oceans*, **123**, 2513–2538, https://doi.org/10.1002/2017JC013464.

Gladish, C. V., D. M. Holland, A. Rosing-Asvid, J. W. Behrens, and J. Boje, 2015: Oceanic boundary conditions for Jakobshavn Glacier. Part I: Variability and renewal of Ilulissat Icefjord waters, 2001–14. *J. Phys. Oceanogr.*, **45**, 3–32, https://doi.org/10.1175/JPO-D-14-0044.1.

Goelzer, H., and Coauthors, 2020: The future sea-level contribution of the Greenland Ice Sheet: A multi-model ensemble study of ISMIP6. *Cryosphere*, **14**, 3071–3096, https://doi.org/10.5194/tc-14-3071-2020.

Harden, B. E., F. Straneo, and D. A. Sutherland, 2014: Moored observations of synoptic and seasonal variability in the East Greenland Coastal Current. *J. Geophys. Res. Oceans*, **119**, 8838–8857, https://doi.org/10.1002/2014JC010134.

Holland, D. M., R. H. Thomas, B. de Young, M. H. Ribergaard, and B. Lyberth, 2008: Acceleration of Jakobshavn Isbræ triggered by warm subsurface ocean waters. *Nat. Geosci.*, **1**, 659–664, https://doi.org/10.1038/ngeo316.

Jackson, R. H., and F. Straneo, 2016: Heat, salt, and freshwater budgets for a glacial fjord in Greenland. *J. Phys. Oceanogr.*, **46**, 2735–2768, https://doi.org/10.1175/JPO-D-15-0134.1.

——, ——, and D. A. Sutherland, 2014: Externally forced fluctuations in ocean temperature at Greenland glaciers in non-summer months. *Nat. Geosci.*, **7**, 503–508, https://doi.org/10.1038/ngeo2186.

——, S. J. Lentz, and F. Straneo, 2018: The dynamics of shelf forcing in Greenlandic fjords. *J. Phys. Oceanogr.*, **48**, 2799–2827, https://doi.org/10.1175/JPO-D-18-0057.1.

——, and Coauthors, 2020: Meltwater intrusions reveal mechanisms for rapid submarine melt at a tidewater glacier. *Geophys. Res. Lett.*, **47**, e2019GL085335, https://doi.org/10.1029/2019GL085335.

Jenkins, A., 2011: Convection-driven melting near the grounding lines of ice shelves and tidewater glaciers. *J. Phys. Oceanogr.*, **41**, 2279–2294, https://doi.org/10.1175/JPO-D-11-03.1.

Kennelly, M., K. Tracey, and D. R. Watts, 2007: Inverted echo sounder data processing manual. University of Rhode Island GSO Tech. Rep. 2007-02, 89 pp., https://doi.org/10.21236/ADA477328.

Khazendar, A., and Coauthors, 2019: Interruption of two decades of Jakobshavn Isbrae acceleration and thinning as regional ocean cools. *Nat. Geosci.*, **12**, 277–283, https://doi.org/10.1038/s41561-019-0329-3.

Li, Q., D. M. Farmer, T. F. Duda, and S. Ramp, 2009: Acoustical measurement of nonlinear internal waves using the inverted echo sounder. *J. Atmos. Oceanic Technol.*, **26**, 2228–2242, https://doi.org/10.1175/2009JTECHO652.1.

Lindeman, M. R., F. Straneo, N. J. Wilson, J. M. Toole, R. A. Krishfield, N. L. Beaird, T. Kanzow, and J. Schaffer, 2020: Ocean circulation and variability beneath Nioghalvfjerdsbræ (79 North Glacier) ice tongue. *J. Geophys. Res. Oceans*, **125**, e2020JC016091, https://doi.org/10.1029/2020JC016091.

Luckman, A., D. I. Benn, F. Cottier, S. Bevan, F. Nilsen, and M. Inall, 2015: Calving rates at tidewater glaciers vary strongly with ocean temperature. *Nat. Commun.*, **6**, 8566, https://doi.org/10.1038/ncomms9566.

Meinen, C. S., R. C. Perez, S. Dong, A. R. Piola, and E. Campos, 2020: Observed ocean bottom temperature variability at four sites in the northwestern Argentine Basin: Evidence of decadal deep/abyssal warming amidst hourly to interannual variability during 2009–2019. *Geophys. Res. Lett.*, **47**, e2020GL089093, https://doi.org/10.1029/2020GL089093.

Mortensen, J., J. Bendtsen, K. Lennert, and S. Rysgaard, 2014: Seasonal variability of the circulation system in a west Greenland tidewater outlet glacier fjord, Godthåbsfjord (64°N). *J. Geophys. Res. Earth Surf.*, **119**, 2591–2603, https://doi.org/10.1002/2014JF003267.

Motyka, R. J., L. Hunter, K. A. Echelmeyer, and C. Connor, 2003: Submarine melting at the terminus of a temperate tidewater glacier, LeConte Glacier, Alaska, U.S.A. *Ann. Glaciol.*, **36**, 57–65, https://doi.org/10.3189/172756403781816374.

——, M. Truffer, M. Fahnestock, J. Mortensen, S. Rysgaard, and I. Howat, 2011: Submarine melting of the 1985 Jakobshavn Isbræ floating tongue and the triggering of the current retreat. *J. Geophys. Res.*, **116**, F01007, https://doi.org/10.1029/2009JF001632.

Oltmanns, M., F. Straneo, H. Seo, and G. W. K. Moore, 2015: The role of wave dynamics and small-scale topography for downslope wind events in southeast Greenland. *J. Atmos. Sci.*, **72**, 2786–2805, https://doi.org/10.1175/JAS-D-14-0257.1.

Pawlowicz, R., B. Beardsley, and S. Lentz, 2002: Classical tidal harmonic analysis including error estimates in MATLAB using t_tide. *Comput. Geosci.*, **28**, 929–937, https://doi.org/10.1016/S0098-3004(02)00013-4.

Roquet, F., G. Madec, T. J. McDougall, and P. M. Barker, 2015: Accurate polynomial expressions for the density and specific volume of seawater using the TEOS-10 standard. *Ocean Modell.*, **90**, 29–43, https://doi.org/10.1016/j.ocemod.2015.04.002.

Sciascia, R., F. Straneo, C. Cenedese, and P. Heimbach, 2013: Seasonal variability of submarine melt rate and circulation in an east Greenland fjord. *J. Geophys. Res. Oceans*, **118**, 2492–2506, https://doi.org/10.1002/jgrc.20142.

Slater, D. A., D. N. Goldberg, P. W. Nienow, and T. R. Cowton, 2016: Scalings for submarine melting at tidewater glaciers from buoyant plume theory. *J. Phys. Oceanogr.*, **46**, 1839–1855, https://doi.org/10.1175/JPO-D-15-0132.1.

——, F. Straneo, S. B. Das, C. G. Richards, T. J. W. Wagner, and P. W. Nienow, 2018: Localized plumes drive front-wide ocean melting of a Greenlandic tidewater glacier. *Geophys. Res. Lett.*, **45**, 12 350–12 358, https://doi.org/10.1029/2018GL080763.

——, ——, D. Felikson, C. M. Little, H. Goelzer, X. Fettweis, and J. Holte, 2019: Estimating Greenland tidewater glacier retreat driven by submarine melting. *Cryosphere*, **13**, 2489–2509, https://doi.org/10.5194/tc-13-2489-2019.

Spall, M., R. H. Jackson, and F. Straneo, 2017: Katabatic wind-driven exchange in fjords. *J. Geophys. Res. Oceans*, **122**, 8246–8262, https://doi.org/10.1002/2017JC013026.

Straneo, F., and P. Heimbach, 2013: North Atlantic warming and the retreat of Greenland's outlet glaciers. *Nature*, **504**, 36–43, https://doi.org/10.1038/nature12854.

——, G. S. Hamilton, D. A. Sutherland, L. A. Stearns, F. Davidson, M. O. Hammill, G. B. Stenson, and A. Rosing-Asvid, 2010: Rapid circulation of warm subtropical waters in a major glacial fjord in east Greenland. *Nat. Geosci.*, **3**, 182–186, https://doi.org/10.1038/ngeo764.

——, R. G. Curry, D. A. Sutherland, G. S. Hamilton, C. Cenedese, K. Våge, and L. A. Stearns, 2011: Impact of fjord dynamics and glacial runoff on the circulation near Helheim Glacier. *Nat. Geosci.*, **4**, 322–327, https://doi.org/10.1038/ngeo1109.

——, and Coauthors, 2012: Characteristics of ocean waters reaching Greenland's glaciers. *Ann. Glaciol.*, **53**, 202–210, https://doi.org/10.3189/2012AoG60A059.

——, G. Hamilton, L. Stearns, and D. Sutherland, 2016: Connecting the Greenland Ice Sheet and the ocean: A case study of Helheim Glacier and Sermilik Fjord. *Oceanography*, **29** (4), 34–45, https://doi.org/10.5670/oceanog.2016.97.

——, and Coauthors, 2019: The case for a sustained Greenland Ice Sheet-Ocean Observing System (GrIOOS). *Front. Mar. Sci.*, **6**, 138, https://doi.org/10.3389/fmars.2019.00138.

Sutherland, D. A., F. Straneo, and R. S. Pickart, 2014: Characteristics and dynamics of two major Greenland glacial fjords. *J. Geophys. Res. Oceans*, **119**, 3767–3791, https://doi.org/10.1002/2013JC009786.

——, and Coauthors, 2019: Direct observations of submarine melt and subsurface geometry at a tidewater glacier. *Science*, **365**, 369–374, https://doi.org/10.1126/science.aax3528.

Watts, D. R., and H. T. Rossby, 1977: Measuring dynamic heights with inverted echo sounders: Results from MODE. *J. Phys. Oceanogr.*, **7**, 345–358, https://doi.org/10.1175/1520-0485(1977)007<0345:MDHWIE>2.0.CO;2.

——, and Coauthors, 2006: Currents, eddies, and a ''fish story'' in the southwestern Japan/East Sea. *Oceanography*, **19** (3), 64–75, https://doi.org/10.5670/oceanog.2006.44.